Magnetic relaxation and three-dimensional critical fluctuations in B-doped Q-Carbon - A high-temperature superconductor

SCHOLARONE™
Manuscripts

Magnetic relaxation and three-dimensional critical fluctuations in B-doped Q-Carbon - A high-temperature superconductor

Anagh Bhaumik[1], Ritesh Sachan[1,2], Jagdish Narayan[1*]

[1]Department of Materials Science and Engineering, Centennial Campus

North Carolina State University, Raleigh, NC 27695-7907, USA

[2]Materials Science Division, Army Research Office, Research Triangle Park, NC 27709, USA

*Correspondence to: narayan@ncsu.edu

Abstract

Dimensional fluctuations and magnetic relaxations in high-temperature superconductors are key considerations for practical applications in high-speed electronic devices. We report the creep of trapped magnetic flux and three-dimensional critical fluctuations near the superconducting transition temperature (T_c = 36 K) in B-doped amorphous Q-carbon. The superconducting phase in B-doped Q-carbon is formed by nanosecond pulsed laser melting in a super undercooled state followed by subsequent quenching. Time-dependent magnetic moment measurements in the B-doped Q-carbon follow Anderson-Kim logarithmic decay model with the calculated value of pinning potential to be 0.75 eV at 1 T near T_c. There is also a strong evidence of three-dimensional (3D) critical fluctuations near T_c in B-doped Q-carbon. The crossover from 2D to 3D critical fluctuations is seen at T/T_c = 1.01 as compared to T/T_c = 1.11 in conventional Bardeen-Cooper-Schrieffer (BCS) high-temperature superconductors. These critical fluctuations indicate moderate to strong electron-phonon coupling in B-doped Q-carbon. The isomagnetic temperature-dependent resistivity measurements reveal a broadening of superconducting

transition width with increasing magnetic field. The upper critical field ($H_{c2}(0)$) is calculated to be 5.6 T using the power law. Finally, the superconducting region is determined in B-doped Q-carbon, as the three vertices of the superconducting region are calculated as $T_c = 36.0$ K, $J_c = 2.9 \times 10^9$ A/cm^2 and $H_{c2} = 5.6$ T. The temperature-dependent magnetic moment and resistivity measurements also validate B-doped Q-carbon as a BCS type-II superconductor. B concentration in Q-carbon can be increased up to 50 at% by nanosecond laser melting and quenching technique, thus providing an ideal platform for near room-temperature superconductivity.

Introduction:

Carbon atoms readily form various allotropes and phases based on its electron configuration. The electronic mixing of sp, sp^2 and sp^3 hybridized states in carbon can lead to a development of several new structures possessing exciting physical and chemical properties.[1,2] In theory, superconductivity in carbon can be achieved owing to its light mass and large Debye frequency, which are the prerequisites for high-temperature superconductivity. However, a weak electron-phonon coupling and low electronic density of states near the Fermi energy level thwart high-temperature superconducting transition in carbon-based materials. Dresselhaus and her coworkers showed (both theoretically and experimentally) that doping (small atoms) in carbon can cause an enhancement of the electron-phonon coupling strength thereby increasing the superconducting transition temperature.[3-5] This concept has led to the evolution of superconductivity in electronically modified carbon-based materials: B-doped diamond (T_c=11 K),[6] alkali-doped fullerene (T_c =33 K),[7] graphene (T_c = 4 K),[8] polycyclic hydrocarbons (T_c =30 K),[9] graphite intercalated materials (T_c =11.5 K),[10] single-walled carbon nanotubes (T_c =15 K),[11] double-walled carbon nanotubes (T_c =7 K)[5] etc. In a nutshell, the superconductivity in carbon-based superconducting materials is caused by a strong electron-phonon mediated pairing of the charge carriers and it follows the well- established BCS formalism.[12] BCS superconductors, unlike oxide superconductors ($YBa_2Cu_3O_{7-\delta}$), can also be interfaced with topological insulators[4] to create Majorana Fermions for quantum computing, sensing and communication.[5] Three important parameters governing the practical applications of a superconductor are: (a) critical current density, (b) upper critical magnetic field, and (c) superconducting transition temperature. There is a loss of the zero-resistance state with an increase in temperature, current or field above a critical limit. Therefore, an increase in the critical current density and upper critical field

without reducing T_c in carbon-based materials will have a profound impact on practical applications, including frictionless motors, high-efficiency power transmission cables, magnetic resonance imaging (MRI), superconducting magnetic energy storage (SMES), electromagnetic pumps and generators, magnetic levitation, *etc.*[13] The critical fluctuations and magnetic relaxations in high-temperature superconductor also play a vital role in the above-mentioned applications.

Superconductivity in B-doped diamond is quite interesting owing to the fact that T_c can be increased from 4 K[14] to 11 K[6] with increasing boron concentration. Theoretical calculations by Cohen and coworkers have predicted T_c in B-doped bulk diamond as high as 80 K with increasing B concentration.[15] However, the increase in the boron concentrations (above ~6 at%) atomic disorder (and compensating defect) in B-doped diamond structure occurs which thwarts T_c.[15] It is observed experimentally that an increase in the B dopant concentration ($n>10^{20}$ cm^{-3}) decreases the activation energy and it exhibits a metal-like behavior.[16] Attaining such high concentrations (beyond thermodynamic solubility limits ~2 at%) by equilibrium Chemical Vapor Deposition (CVD) techniques poses a major challenge. The non-equilibrium technique, plasma enhanced CVD (PECVD) was used to increase the B at% up to 6%, after which it started to form B-dimers.[6] The formation of B-dimers leads to the symmetric and anti-symmetric combinations of bound states of boron thereby reducing the value of T_c.[17] We are able to overcome the above-mentioned challenges of B-doping by using non-equilibrium laser-assisted melt quenching technique. We have reported the formation of Q-carbon (quenched-carbon) by nanosecond pulsed laser melting of amorphous carbon in a super undercooled state and subsequent quenching of the molten carbon layers.[18-21] The molten carbon in the super undercooled state has metallic bonding, which promotes close-packing of carbon atoms, and upon quenching sp^3

tetrahedra are formed. The sp^3 bonded carbon tetrahedra are randomly distributed, creating amorphous Q-carbon. Most of these tetrahedral can have sp^3 bonded B atoms. The carbon in the interfacial region between the tetrahedral is sp^2 bonded and B in this region is also sp^2 bonded. Similar conversion of h-BN to c-BN and Q-BN is also observed using the pulsed laser annealing (PLA) technique.[22] The Q-carbon consists of a phase mixture of sp^3 (>80%) and rest sp^2 bonded carbon atoms and it can exist in Q1, Q2, and Q3 polyamorphic states.[18,23] This novel material exhibits interesting properties, such as low electron affinity in electric field, room-temperature ferromagnetism in undoped state, significantly enhanced *hardness* than diamond etc.[18,21,24]

In the present study, we employ the PLA technique on the B/amorphous C multilayer structures to synthesize B-doped Q-carbon, where we can exceed B doping beyond thermodynamic solubility limits (17.0±1.0 at% and higher) by adjusting the relative thickness of B/C composite layers. This leads to a high-temperature superconductivity (T_c = 36 K) in B-doped Q-carbon. Recently, Sakai *et al.* have theoretically predicted T_c = 37 K in B-doped Q-carbon at 14 at% B-doping and confirmed our experimental results, including the enhancement in the density of states near the Fermi level.[25] We examine the BCS superconductivity in B-doped Q-carbon using temperature and field dependent magnetic and electrical measurements. According to the BCS formalism, Cooper pairs are formed below T_c, which move in zero-resistive paths in superconducting materials. This is caused by the emergence of shallow-level energy states near Fermi level below T_c. This leads to a zero-resistance conduction in superconducting materials which have potential applications ranging from frictionless motors and high-efficiency power transmission cables to superconducting qubits. The superconducting creep measurements (time-dependent magnetic moment) are performed in a superconducting quantum interference device. Critical fluctuation measurements are performed in physical property measurement system. The

electronic structure, vibrational modes and morphology of B-doped Q-carbon are characterized by electron-energy-loss spectroscopy (EELS) in a scanning transmission electron microscope (STEM), Raman spectroscopy and scanning electron microscopy (SEM). Finally, we discuss the origin and nature of superconductivity in B-doped Q-carbon using the BCS formalism.

Experimental:

Pulsed laser deposition (PLD) technique is used to deposit alternating layers of boron and amorphous carbon thin films onto c-sapphire with a thickness ranging from 100-500 nm in the temperature range of 30-300 ^{o}C and 1.0×10^{-6} Torr operating pressure. During the deposition process the pulsed laser beam (KrF excimer laser having laser wavelength=248 nm, pulse duration=25 ns and energy density=3.0 Jcm^{-2}) is rastered through the carbon and boron (sector) targets. Both the targets are mounted on the same target holder during the PLD process. Subsequently, these B-doped amorphous carbon thin films (grown by PLD technique) are irradiated with nanosecond ArF excimer laser (laser wavelength=193 nm, pulse duration=20 ns) using laser energy density 0.6-1.0 Jcm^{-2}. The pulsed laser annealing (PLA) technique melts the B-doped amorphous carbon film in a highly super undercooled state, and quenched rapidly. The whole process is completed within 200-250 ns. This leads to conversion of amorphous carbon films into B-doped quenched carbon structure where B is doped beyond thermodynamic solubility limit *via* solute trapping. The undercooling is controlled by thermal conductivities of the substrate (sapphire in this case) and as-deposited diamond-like carbon thin films and laser parameters (laser energy density (0.6-1.0 J/cm^2), laser wavelength (193 nm) and pulsed laser width (20 ns)). The thermal conductivities of the as-deposited diamond-like carbon thin films can be controlled by varying the ratio of sp^2/sp^3 -hybridized carbon. The formation of B-doped Q-carbon is dependent on the laser parameters and physical properties of the substrate, which

6

control the solidification velocity. The solidification velocity (v) is directly related to the

undercooling by the equation: $v = \frac{D_\propto f}{\lambda f_D}\left(1 - e^{\frac{(T_m - T_u)\Delta S}{kT}}\right)$, where, $D_\propto, f, \lambda, \ f_D, k, T, T_m, T_u$ and ΔS

denote the diffusivity of the amorphous carbon ($\sim 10^{-8}$ m^2/sec in liquid state), fraction of the

available sites, atomic jump distance, geometrical factor associated with diffusion, Boltzmann

constant, temperature, melting temperature, undercooling temperature, and the change in

entropy, respectively. An increase in the value of T_u decreases the value of chemical free energy

barrier for carbon to amorphous B-doped Q-carbon phase transformation. This also increases the

velocity of the melt front. Therefore, the values of undercooling dictate the production of Q-

carbon from the carbon melt. If the cooling rate is slow (low undercooling and low solidification

velocity ((~5 m/sec))), nano and microdiamonds are formed whereas with high cooling rates

(large undercooling and large solidification velocity (>10 m/sec)) amorphous Q-carbon is

formed.[18,23,26-29] At intermediate velocities, a composite of Q-carbon and diamond is formed. The

characterization of the B-doped Q-carbon phase was carried out using Raman spectroscopy,

electron energy-loss spectroscopy (EELS), field emission scanning electron microscopy

(FESEM) and superconducting quantum interference device (SQUID) magnetometry. To

characterize the Raman active vibrational modes, Alfa300 R superior confocal Raman

spectroscope with a lateral resolution less than 200 nm was employed. Crystalline Si was used to

calibrate Raman spectra, which has its characteristic Raman active peak at 520.6 cm^{-1}. High-

resolution SEM with sub-nanometer resolution was carried out using FEI Verios 460L SEM to

characterize the laser-irradiated (B-doped Q-carbon) films. To prepare the crosssectional

transmission electron microscope (TEM) samples, a FEI Quanta 3D FEG instrument having dual

beam technology employing both electron and ion beam guns, was used. A low energy ion beam

(5 kV, 10 pA) was used to cleanup the focused ion beam (FIB) surface damage. Aberration-

corrected STEM-FEI Titan 80-300 was used in conjunction with EELS to acquire high-angle

annular dark-field (HAADF) images and EELS spectra of B-doped Q-carbon thin films. The

electron probe current used in the experiment was 38±2 pA. The EELS data was acquired with a

collection angle of 28 mrads. Quantum design magnetic property measurement system (MPMS3)

was used to measure temperature, field and time-dependent magnetic properties of thin films.

Both the vibrating sample magnetometry (VSM) and direct current (DC) modes were used for

measuring field, time and temperature-dependent magnetization. The magnetic flux-creep

measurements were performed at isothermal conditions (up to 5000 secs) and magnetic field of 1

T after attainment of zero field conditions. The magnetic measurements were made with samples

mounted parallel to the magnetic field. The temperature and field dependent resistivity

measurements were performed in the physical property measurement system (PPMS).

Results and discussion:

A. Temperature-dependent magnetic studies: Figure 1(a) depicts temperature-dependent

magnetic moment plots of B-doped Q-carbon at zero field cooled (ZFC) and field cooled (FC)

conditions. As it is evident from the plots that there is an expulsion of magnetic field (Meissner

diamagnetism) below the superconducting transition temperature (T_c) in B-doped Q-carbon.

There is a sharp onset of diamagnetism at 36.0±0.5 K with complete diamagnetic shielding at

lower temperatures. There also occurs penetration of the magnetic field with an increase in the

applied magnetic field in the field cooled conditions, which results in the upward shift of the

magmetic moment curves below T_c. The temperature-dependent difference in the magnetic

moment ($\Delta M = M_{FC} - M_{ZFC}$) at different applied magnetic field (20 Oe and 80 Oe) are shown as an

inset in figure 1(a). There is a drastic difference between the temperature dependence of ΔM

below and above T_c. Above T_c, there is no temperature dependence of ΔM, thereby indicating a

complete destruction of superconductivity (destruction of Josephson coupling) in B-doped Q-carbon. It should also be noted that ΔM increases with increasing applied magnetic field (below upper critical magnetic field). This suggests pinning of the magnetic vortices in the B-doped Q-carbon structure. The magnetic susceptibility (χ) of B-doped Q-carbon samples are calculated as ~ -0.02 and -0.09 emu $cc^{-1}Oe^{-1}$ for FC and ZFC (at 5 K), respectively (inset of figure 1(a)). The ZFC magnetization shows the flux exclusion from the B-doped Q-carbon sample, whereas the FC magnetization indicates the flux expulsion. The shielding fraction is calculated from the ZFC curve whereas the superconducting volume fraction is calculated from the FC curve. A drastic difference between the ZFC and FC curves indicates pinning of the magnetic vortices in B-doped Q-carbon. The ZFC susceptibility ($-4\pi \chi$) represents the shielding fraction in a superconducting material. A complete shielding ($4\pi \chi < -1$) is observed in the B-doped Q-carbon samples, which indicates a high-quality superconducting phase. The superconducting volume fraction (Meissner fraction) is calculated from the FC curve at low applied magnetic field ($H < H_{c1}$). Without considering the demagnetization enhancement factor, the superconducting volume fraction is calculated to be ~25 %. Figures 1(b) and (c) show the temperature-dependent normalized first derivative of magnetic moment and second derivative of magnetic moment, respectively. The derivative method provides line shapes, characteristics peaks and crossover points which determine characteristic superconducting parameters.[30] The pronounced peak (T_c) and FWHM (ΔT) are observed at 35.5 K and 3.0 K, respectively. In figure 1(c), the temperature at which the curve crosses the zero line indicates T_c. The peak to peak width ($\Delta T^{/}$) is calculated to be 0.5 K. The ratio of the widths calculated from the derivative plots ($\Delta T /\Delta T^{/}$) is 6.0 and it indicates the characteristic of the superconducting transition line shape. The assymetry of the transition is calculated to be 4.9×10^{-3} using the relation: (A-B)/(A+B). The line shape and asymmetry of the

superconducting transition in B-doped Q-carbon indicate the presence of moderate electron-phonon coupling in this material.[30]

B. Electron Microscopy: The high-resolution electron microscopy, electron energy loss spectroscopy (EELS) and unpolarized Raman spectroscopy of B-doped Q-carbon are shown in figure S1. The super undercooling process results in interfacial instability thereby forming the filamentary structure of B-doped Q-carbon (figure S1(a)).[31] Figure S1(b) shows the room-temperature unpolarized Raman spectroscopy of B-doped Q-carbon indicating a sp^3 fraction ~84%, which is in excellent agreement with core-loss EELS (figure S1(d)). B-doped Q-carbon forms on c-sapphire (substrate) and is evident from the cross-sectional HAADF image (figure S1(c)). A uniform distribution of B in Q-carbon is also observed which has been reported earlier.[31] B concentration is also estimated (using a quantitative approach)[32] to be 17.0±1.0 at% in B-doped Q-carbon [26,31] (please see supplementary information for details).

C. Calculation of Critical fields: The critical fields in B-doped Q-carbon superconducting phase are calculated using temperature dependent resistivity (at various magnetic field) and field-dependent magnetic moment (at various temperatures) measurements and the results are shown in figure 2. There is a sharp drop in the normalized resistivity ($\rho(T)/\rho(300)$) below T_c in B-doped Q-carbon (shown in figure 2(a)). This sharp transition is also indicative of homogeneous superconductivity in this material. Higher magnetic fields are required to destroy the superconducting nature of B-doped Q-carbon, as it is evident from the lowering of T_c and broadening of transition width with increasing magnetic field. The temperature corresponding to the zero-resistivity point vs magnetic field is shown as an inset in figure 2(a). To estimate the upper critical field (H_{c2}), the plot is extrapolated using the equation: $\frac{H_c(T)}{H_c(0)} = 1 - (\frac{T}{T_c})^2$. The value of $H_{c2}(0)$ is calculated to be 5.6 T. The inset of figure 2(b) indicates an irreversible nature of the

magnetic moment with increasing and decreasing magnetic field. This is attributed to

intergranular and London currents (around the superconducting grains), which can trap the

Abrikosov vortices and fluxons in an irreversible manner thereby causing a hysteresis behavior

of the magnetic moment *vs* field plots.[33] Above T_c, there is a complete loss of the hysteresis

behavior indicating a complete dissolution of the Joshepson coupling in the superconducting

grains of B-doped Q-carbon. As it is evident from the figure 2(b) that there is a decrease in the

absolute value of magnetic moment with increasing temperature, a characteristic of

superconducting materials.[34] The plots also indicate type-II superconductivity in B-doped Q-

carbon, having distinct values of lower critical field (H_{c1}) and H_{c2} below T_c. The H_{c1} and H_{c2} are

calculated from the point (magnetic field) at which the moment reaches its minimum value and

the field at which M(H) first deviates from the background, respectively. The values of $H_{c1}(0)$

and $H_{c2}(0)$ are calculated as 0.1 and 5.4 T, respectively. The anomalous drop of the lower critical

field at low temperature[26] requires further theoretical and experimental research (in B-doped Q-

carbon which is currently underway). A similar drop in the lower critical field at low

temperatures is also reported in amorphous carbon doped with sulphur.[35] The Ginzburg-Landau

parameter (k) is calculated to be 1.04 using the equation: $\frac{H_{c1}(0)}{H_{c2}(0)} = \frac{\ln(k)}{k^2 \times 2\sqrt{2}}$.[33] The detailed

calculations are shown in the supplementary information (figure S2). Since the value of k

$>1/\sqrt{2}$, it shows that B-doped Q-carbon is a type-II superconductor. Figure 2(c) shows

magnetization hysteresis loop at various temperatures (2, 11 and 21 K) below T_c. As it is evident

from the hysteresis loops that there is irreversibility of the magnetization curves. This is due to

pining of flux lines. The inset in figure 2(c) shows the irreversibility of the magnetization curves

at 2 K. This results in a width (difference in M+ and M- values) which gives rise to critical

current density. Addition of extrinsic impurities in superconductors increases the value of critical

11

current density. But in the case of B-doped Q-carbon superconductor, there exists B-doped sp^2

hybridized carbon (non-superconducting entities) as pinning centers without adversely affecting

T_c. Figure 2(d) depicts the critical fluctuations in B-doped Q-carbon. The figure indicates the

presence of short-wave fluctuations (n=-3.5), mean-field region (n=-1 and -0.5), and critical

region (n=-0.2). These characteristics explicitly explain the curvature of the resistivity plot near

T_c.[36] In the mean-field region (using Aslamazov-Larkin equation) the reduced conductivity

$(\sigma'=\Delta\sigma/\sigma_0)$ is expressed using the equation: $\frac{\Delta\sigma}{\sigma_0} = (AT')^n$,[37] where σ_0 is the conductivity at 300

K, $\Delta\sigma$ is the difference between room temperature conductivity and conductivity at a particular

temperature, A is the temperature independent constant, n is the critical exponent ($n = -0.5$ and -

1.0 for 3D and 2D critical fluctuations, respectively) and T' is the reduced temperature defined

using the relation: $T' = (^T/_{T_c} - 1)$. The critical fluctuations occur close to T_c and the

dimensionality of the fluctuations (2D or 3D) are important superconducting parameters. There

is a transition from 2D to 3D nature of critical fluctuation near T_c in B-doped Q-carbon. The 2D

to 3D crossover is seen at $T/T_c = 1.01$ as compared to $T/T_c = 1.11$ in other high-temperature

superconductors.[35] Similar 3D fluctuations are seen in other high-temperature superconductors:

YBCO, LSCO.[36] These fluctuations indicate moderate to strong electron-phonon coupling in the

superconducting state.

D. Superconducting regime: Figure 3 depicts the superconducting region in B-doped Q-carbon,

which is enclosed by T_c, H_{c2} and critical current density (J_c). The values of J_c are calculated

using the Bean's formula: $J_c = \left[\frac{20\Delta M}{tw^2\left(l-\frac{w}{3}\right)} \right]$, where ΔM is the difference in magnetization values

(+M and -M) at a particular magnetic field, and t, w, and l are the thickness, width and length,

respectively, of the B-doped Q-carbon sample. As it is evident from the J_c plots that there is a

sharp decrease in the value of J_c with an increase in the applied magnetic field, characteristic of a superconducting material. A weaker field dependence of J_c at higher fields are also seen in B-doped Q-carbon due to the presence of weakly connected superconducting grains. The value of J_c (0 Oe) at 2 K is calculated as 2.7×10^9 A/cm^2, which is considerably higher than oxide high-temperature superconductors.[38,39] The high values of critical current density may be due to unique pinning state associated with mixing of sp^3 and sp^2 bonding in B-doped Q-carbon thin film.[40] For the practical applications of superconductors, there is a necessity to increase J_c which facilitates larger superconducting region for the flow of dissipationless current. An increase in J_c is also conducive to lower flux creep rate, which is a key to frictionless motors and other superconducting applications. Previous reports indicate that there is a considerable increase in J_c with the introduction of extrinsic defects.[41] These processes reduce T_c of the material and thereby effectively reducing the superconducting region (volume). In the case of B-doped Q-carbon due to the ultrafast laser melting and subsequent quenching process, the structure is densely packed. This leads to an increase in the density of electronic states near Fermi level which facilitates high values of T_c and J_c. The large values of J_c at low temperature (2 K) are due to the presence of pinned states in the structure of B-doped Q-carbon. The B-doped Q-carbon contains an electronic mixture of sp^3 (~80%) and rest sp^2 hybridized carbon atoms. The superconductivity in this material is due to the formation of hole Cooper pairs, which are generated when boron is doped in the C- sp^3 hybridized structure. The presence of B-doped C- sp^2 entities in B-doped Q-carbon can increase the values of J_c by introducing the pinning centers. At higher magnetic fields these pinned states can move thereby drastically reducing the values of J_c. Above the irreversibility field (H^*), the Lorentz forces on the magnetic vortices are large enough to facilitate their detachment from the pinning sites.[42] This causes a reduction in the ability of a high-temperature

superconductor to carry dissipation-free current. The value of H^* is calculated to be ~2.5 T

which is approximately half of $H_{c2}(0)$. A reduction of grain size in superconductors is also a

viable path for increasing J_c.[42] The size of the superconducting grains is comparable to the ε_L in

B-doped Q-carbon. The low grain size can also causes a tremendous increase in the value of J_c in

B-doped Q-carbon. Figure 3 also shows temperature-dependent J_c measurements in B-doped Q-

carbon. These data points correspond to the value of J_c at a particular temperature at 0 Oe. There

is a charateristic drop of J_c with an increase in temperature and can be fitted with the equation:

$\frac{J_c(T)}{J_c(0)} = 1 - (\frac{T}{T_c})$. The magnetic field-dependent temperature measurements are also shown in the

figure 3. These measurements illustrate the characteristic nature of superconductivity in B-doped

Q-carbon. Three vertices of the figure 3 illustrate T_c (36.0 K), J_c (2.9×10^9 A/cm^2) and H_{c2} (5.6

T), which are the three important parameters of a superconducting material. The values of critical

current density are 2.20×10^8 and 1.72×10^8 A/cm^2 at 1T (10 K) and 2T (10 K), respectively. At

1T the values of critical current density are 2.37×10^8 and 2.20×10^8 A/cm^2 at 5 and 10 K,

respectively. The high values of critical current density and T_c will enable B-doped Q-carbon

power transmission (superconducting) cables to carry a large amount of dissipation-less current.

For example, a YBCO superconductor carrying a 150 A current (below T_c) can lead to an

eightfold reduction of the heat load as compared to pristine Cu (in oxygen-free environment

under similar operating conditions).[13] Therefore, the use of B-doped Q-carbon in power

transmission and superconducting magnets will drastically decrease transmission losses (in the

form of resistive heat) and cost of materials processing (carbon-based material). The large values

of H_{c2} in B-doped Q-carbon will also facilitate its use in superconducting supercolliders

operating at liquid He temperature. B-doped Q-carbon will also find its application in He-based

close-cycle refrigeration systems, operating above 10 K. This novel carbon-based material can

also be used in MRI systems, where magnetic flux densities of ~2T are used. Since B-doped Q-carbon has high values of T_c, J_c and H_{c2}, it can sustain high magnetic fields and can also simplify cryogenic apparatus. These factors ultimately reduce the operational cost of superconducting-based frictionless motors. Electromagnetic pumping can also be achieved by using B-doped Q-carbon as electrodes. These superconducting pumps have no moving (mechanical) parts and work on the reactive thrust principle which helps in fluid propulsion.[43] The large superconducting regime in B-doped Q-carbon shows that it can also be used in SMES devices (which can supply transient power at switching stations in a MAGLEV track) where the magnetic energy is stored in a superconducting coil energized with a circulating dissipation-less current. The use of B-doped Q-carbon as interconnects will also reduce propagation delays ($\approx$ resistance×capacitance) between the electronic devices, thereby increasing the versatility of superconducting applications of B-doped Q-carbon. Since B-doped Q-carbon is totally biocompatible, it can be used for implantable devices.

E. Time-dependent magnetic moment: Figure 4 depicts the time-dependent magnetic moment (flux creep) measurements in B-doped Q-carbon. The flux creep phenomenon follows the Anderson-Kim logarithmic time dependence[44] (shown up to 5000 sec) with the reduced magnetic moment ($M(t)/M(t=0)$), as shown in figure 4(a). The motion of the pinned magnetic fluxes is associated with the flux creep which can be activated thermally. The probablity of the thermally activated jumps increases exponentially with an increase in temperature. Thermally activated creep mechanism leads to dampening of supercurrents and reduction of magnetization, which thwart the high-temperature (below T_c) use of superconductors. The time-dependent magnetic moment data can be fitted using the equation: $\frac{M(t)}{M(t=0)} = 1 - S \times \ln(1 + \frac{t}{\tau_0})$,[44] where τ_0 denotes

the time constant and $S = k_B T \big/ U_p$. The fitted plots are shown in the figure 4(a) for various

values of T/T_c. The important parameters governing the flux creep phenomenon are the pinning

potential (U_p), isothermal magnetization relaxation (S), and τ_0. The flux creep measurements are

performed at a high magnetic field (1 T, field below upper critical field) which facilitate a strong

interaction between the dense magnetic vortices. These measurements, therefore, yield better

results of the pinning parameters related to the inter-vortex interaction phenomena. Figure 4(b)

indicates an exponential dependence of the magnetic relaxation with temperature. The

exponenential relation between S and T_c is calculated as: $S \approx (e^{T/0.16T_c})$. This is associated with

the average velocity of the thermally activated jumps (of magnetic flux lines) which is also

exponentially related to the temperature. The inset in figure 4(b) shows the temperature-

dependent change in magnetization loop width (ΔM). It shows a decrease in ΔM with

temperature (up to T_c) which also causes a decrease in the pinning potential. The isothermal

magnetic relaxation studies in B-doped Q-carbon indicate a strong flux creep near T_c. The strong

thermal fluctuations near T_c cause a giant creep of magnetic vortices and create a vortex liquid

state. This reduces the effective pinning potential, as shown in figure 4(c). There is a complete

reduction of the trapped flux (vortex state) above T_c (normal state). Unlike in YBCO, where the

pinning centers are formed due to the presence of dislocations in the CuO_x layers,[45] in B-doped

Q-carbon the B-doped sp^2 hybridized carbon entities may form the effective pinning centers. The

pinning potential increases with decreasing temperature (as shown in figure 4(c)). The value of

U_p near T_c is calculated as 0.75 eV, which is comparable to that in commercially available high-

temperature superconductors (such as non-BCS YBCO).[45] Figure 4(c) also shows the

temperature-dependent time constant measurements in B-doped Q-carbon. The τ_0 determines a

transient state before the onset of the logarithmic magnetic relaxation (figure 4(a)). A transient

time of ~300 sec is registered at temperatures close to T_c which indicates a superior

superconducting behavior of B-doped Q-carbon. As it is evident from the figure 4(a) that there is

only ~1.2% decrease in magnetic moment at T/T_c=0.97, which indicates an immense

applicability of B-doped Q-carbon in MRI and NMR inserts. A much higher change in magnetic

moment (~20%) is seen in other high-temperature superconductors due to the formation of a

frustated glassy state.[46] The magnetic flux lines extend over a distance approximately equal to

the London penetration depth in B-doped Q-carbon. The free energy barrier (ΔF near 0 K) of the

flux bundle can be calculated as 688.02 T^2 nm^3 using the equation: $\Delta F = (\frac{H_{c2}(0)^2}{8\pi})\lambda_L^3$.[47] The high

values of critical current density (at low temperatures) in B-doped Q-carbon can be correlated

with large values of free-energy barrier and pinning potential in its structure. The large pinning

potential (in superconductors) is a critical criterion for levitation and MRI applications.[46] It

should also be noted that the flux pinning strength and dimension of the critical fluctuations

(near T_c) determine the irreversibility (hysteresis) of the M-H loops. In B-doped Q-carbon, the

3D nature of critical fluctuations and a high pinning potential result in the butterfly-like hystersis

(in the M-H plots), indicating superior superconducting characteristics of B-doped Q-carbon.

Conclusions

In conclusion, we presented the magnetic relaxation and three-dimensional critical fluctuations in

a high-temperature superconductor: B-doped Q-carbon. These studies will eventually lead to the

formation of commercially viable B-doped Q-carbon-based thermoelectric and various other

superconducting devices. This superconducting phase is formed as a result of nanosecond laser

melting in a super undercooled state and subsequent quenching of a amorphous carbon and boron

composite layers. A sharp onset of diamagnetism is observed in B-doped Q-carbon at 36.0±0.5 K

with complete diamagnetic shielding at lower temperatures (below T_c). The magnetization vs temperature measurements also indicate similar results. There occurs a penetration of the magnetic field (with an increase in the applied magnetic field) in the field-cooled conditions, which results in the upward shift of the magnetic moment curves below T_c. The temperature-dependent resistivity measurements indicate an abrupt drop of resistivity below T_c in B-doped Q-carbon. This sharp transition is indicative of homogeneous superconductivity in this material, which is possible due to the absence of B clusters in B-doped Q-carbon. The field-dependent resistivity vs temperature plots indicate that a large magnetic field is required to destroy the superconducting nature of B-doped Q-carbon. With increasing magnetic field, there is a lowering of T_c and subsequent broadening of the transition width in B-doped Q-carbon. Critical fluctuations measurements in B-doped Q-carbon show a transition from 2D to 3D (nature of critical fluctuation) near T_c, which plays an important role in the superconducting transition. Using the power law, the value of $H_{c2}(0)$ is calculated to be ~ 5.6 T from the resistivity and magnetic plots. The magnetic moment vs field plots at various temperatures (below T_c) indicate an irreversible nature of the magnetic moment with increasing and decreasing magnetic field. This is due to the fact that intergranular and London currents (around the superconducting grains) can trap the Abrikosov vortices and fluxons in an irreversible manner, thereby causing a hysteresis behavior of the magnetic moment vs field plots in B-doped Q-carbon. Finally we have also shown that the large values of J_c (~2.7×10^9 A/cm^2) at low temperatures (~2 K), which are attributed to the presence of pinned states in the structure of B-doped Q-carbon. To calculate the pinning potential in B-doped Q-carbon we have performed time-dependent isothermal magnetic moment studies, which follow Anderson-Kim logarithmic decay formalism. The values of pinning potential and transient time near T_c are calculated to be 0.75 eV and ~300 sec,

respectively, indicating superior superconducting properties of B-doped Q-carbon. Isothermal magnetic relaxation studies in B-doped Q-carbon also indicate a strong flux creep near T_c. Structural characterizations using Raman spectroscopy and EELS indicate a high sp^3 fraction (~84%) and rest sp^2 in the B-doped Q-carbon phase. The B-doped sp^2 hybridized carbon (non-superconducting entities), which is present in the B-doped Q-carbon, may act as effective pinning sites thereby increasing the values of pinning potential (near T_c), critical current density and upper critical field in this material. The motion of fluxoids in thermal gradients causes electromagnetic force (*e.m.f*) in a type-II superconductor. This leads to generation of potential difference, thereby leading to design of better thermoelectric devices (non-zero Peltier and Thompson coefficients). We have successfully demonstrated the motion of the fluxoids (by varying temperature and pinning potential) in B-doped Q-carbon. Since B-doped Q-carbon is a BCS (*s*-wave) superconductor unlike oxide superconductors, it can be interfaced with topological insulators[48] to create Majorana Fermions[49] for quantum computing, sensing and secure communication applications. This discovery of high-temperature superconductivity in B-doped Q-carbon will stimulate further research in carbon-based superconductivity. Recent measurements show higher T_c with increasing boron concentration. We have synthesized B-doped Q-carbon with B concentration close to 50%, and estimated T_c over 114 K.

Acknowledgements

References

1   M. S. Dresselhaus and G. Dresselhaus, *Nanostructured Mater.*, 1997, **9**, 33–42.

2   J. Narayan, V. P. Godbole and C. W. White, *Science*, 1991, **252**, 416–8.

3   R. A. Jishi and M. S. Dresselhaus, *Phys. Rev. B*, 1992, **45**, 12465–12469.

4   R. A. Jishi and M. S. Dresselhaus, *Phys. Rev. B*, 1992, **45**, 2597–2600.

5   W. Shi, Z. Wang, Q. Zhang, Y. Zheng, C. Ieong, M. He, R. Lortz, Y. Cai, N. Wang, T. Zhang, H. Zhang, Z. Tang, P. Sheng, H. Muramatsu, Y. A. Kim, M. Endo, P. T. Araujo and M. S. Dresselhaus, *Sci. Rep.*, 2012, **2**, 625.

6   H. Okazaki, T. Wakita, T. Muro, T. Nakamura, Y. Muraoka, T. Yokoya, S. Kurihara, H. Kawarada, T. Oguchi and Y. Takano, *Appl. Phys. Lett.*, 2015, **106**, 52601.

7   K. Tanigaki, T. W. Ebbesen, S. Saito, J. Mizuki, J. S. Tsai, Y. Kubo and S. Kuroshima, *Nature*, 1991, **352**, 222–223.

8   A. Di Bernardo, O. Millo, M. Barbone, H. Alpern, Y. Kalcheim, U. Sassi, A. K. Ott, D. De Fazio, D. Yoon, M. Amado, A. C. Ferrari, J. Linder and J. W. A. Robinson, *Nat. Commun.*, 2017, **8**, 14024.

9   M. Xue, T. Cao, D. Wang, Y. Wu, H. Yang, X. Dong, J. He, F. Li and G. F. Chen, *Sci. Rep.*, 2012, **2**, 389.

10   T. E. Weller, M. Ellerby, S. S. Saxena, R. P. Smith and N. T. Skipper, *Nat. Phys.*, 2005, **1**, 39–41.

11   Z. K. Tang, L. Zhang, N. Wang, X. X. Zhang, G. H. Wen, G. D. Li, J. N. Wang, C. T. Chan and P. Sheng, *Science (80-.).*, 2001, **292**, 2462–2465.

12   N. Emery, C. Hérold, M. d'Astuto, V. Garcia, C. Bellin, J. F. Marêché, P. Lagrange and

      G. Loupias, *Phys. Rev. Lett.*, 2005, **95**, 87003.

13   A. Bourdillon and N. X. Tan Bourdillon, *High temperature superconductors : processing

      and science*, Academic Press, 1994.

14   E. A. Ekimov, V. A. Sidorov, E. D. Bauer, N. N. Mel'nik, N. J. Curro, J. D. Thompson

      and S. M. Stishov, *Nature*, 2004, **428**, 542–545.

15   J. E. Moussa and M. L. Cohen, *Phys. Rev. B*, 2008, **77**, 64518.

16   T. Klein, P. Achatz, J. Kacmarcik, C. Marcenat, F. Gustafsson, J. Marcus, E. Bustarret, J.

      Pernot, F. Omnes, B. E. Sernelius, C. Persson, A. Ferreira da Silva and C. Cytermann,

      Phys. Rev. B, 2007, **75**, 165313.

17   B. Šopík and P. Lipavský, *Diam. and Rel. Mat.* 2012, **21**, 77.

18   J. Narayan and A. Bhaumik, *J. Appl. Phys.*, 2015, **118**, 215303.

19   J. Narayan and A. Bhaumik, *APL Mater.*, 2015, **3**, 100702.

20   A. Bhaumik and J. Narayan, *JOM*, 2018, **70**, 456–463.

21   J. Narayan, S. Gupta, A. Bhaumik, R. Sachan, F. Cellini and E. Riedo, *MRS Commun.*,

      2018, 1–9.

22   J. Narayan and A. Bhaumik, *APL Mater.*, 2016, **4**, 20701.

23   J. Narayan, A. Bhaumik and R. Sachan, *J. Appl. Phys.*, 2018, **123**, 135304.

24   A. Bhaumik, S. Nori, R. Sachan, S. Gupta, D. Kumar, A. K. Majumdar and J. Narayan,

      ACS Appl. Nano Mater., 2018, **1**, 807–819.

25   Y. Sakai, J. R. Chelikowsky and M. L. Cohen, *Phys. Rev. B*, 2018, **97**, 54501.

26   A. Bhaumik, R. Sachan and J. Narayan, *J. Appl. Phys.*, 2017, **122**, 45301.

27   J. Narayan, A. Bhaumik, S. Gupta, A. Haque and R. Sachan, *Mater. Res. Lett.*, 2018, **6**,

353–364.

28   S. Gupta, R. Sachan, A. Bhaumik, P. Pant and J. Narayan, *MRS Commun.*, 2018, 1–8.

29   S. Gupta, A. Bhaumik, R. Sachan and J. Narayan, *JOM*, 2018, 1–6.

30   C. Almasan, J. Estrada, C. P. Poole, T. Datta, H. A. Farach, D. U. Gubser, S. A. Wolf and

L. E. Toth, *MRS Proc.*, 1987, **99**, 451.

31   A. Bhaumik, R. Sachan and J. Narayan, *ACS Nano*, 2017, **11**, 5351–5357.

32   R. Sachan, V. R. Cooper, B. Liu, D. S. Aidhy, B. K. Voas, M. Lang, X. Ou, C.

Trautmann, Y. Zhang, M. F. Chisholm and W. J. Weber, *J. Phys. Chem. C*, 2017, **121**,

975–981.

33   A. P. Drozdov, M. I. Eremets, I. A. Troyan, V. Ksenofontov and S. I. Shylin, *Nature* 2015,

525, 73.

34   A. Bhaumik, R. Sachan, S. Gupta and J. Narayan, *ACS Nano*, 2017, **11**, 11915–11922.

35   I. Felner and Y. Kopelevich, *Phys. Rev. B*, 2009, **79**, 233409.

36   N. Sudhakar, M. K. Pillai, A. Banerjee, D. Bahadur, A. Das, K. P. Gupta, S. V. Sharma

and A. K. Majumdar, *Solid State Commun.*, 1991, **77**, 529–533.

37   L. G. Aslamasov and A. I. Larkin, *Phys. Lett. A*, 1968, **26**, 238–239.

38   W. S. Yang, J. H. Noh, N. J. Jeon, Y. C. Kim, S. Ryu, J. Seo and S. I. Seok, *Science* 2015,

348, 1234–1237.

39   Y. Zhang, S. Johnson, G. Naderi, M. Chaubal, A. Hunt and J. Schwartz, *Supercond. Sci.

Technol.*, 2016, **29**, 95012.

40   S.-G. Jung, J.-H. Kang, E. Park, S. Lee, J.-Y. Lin, D. A. Chareev, A. N. Vasiliev and T.

Park, *Sci. Rep.*, 2015, **5**, 16385.

41   M. Baert, V. V. Metlushko, R. Jonckheere, V. V. Moshchalkov and Y. Bruynseraede,

Phys. Rev. Lett., 1995, **74**, 3269–3272.

42   Y. Bugoslavsky, L. F. Cohen, G. K. Perkins, M. Polichetti, T. J. Tate, R. Gwilliam and A. D. Caplin, *Nature*, 2001, **411**, 561–563.

43   K. X. Qian, S. S. Wang and S. H. Chu, *ASAIO J.*, **39**, M649-53.

44   T. Scheike, W. Böhlmann, P. Esquinazi, J. Barzola-Quiquia, A. Ballestar and A. Setzer, *Adv. Mater.*, 2012, **24**, 5826–5831.

45   V. Y. Monarkha, A. G. Sivakov and V. P. Timofeev, *Low Temp. Phys.*, 2014, **40**, 861–863.

46   Y. Yeshurun, A. P. Malozemoff and A. Shaulov, *Rev. Mod. Phys.*, 1996, **68**, 911–949.

47   P. W. Anderson and P. W., *Phys. Rev. Lett.*, 1962, **9**, 309–311.

48   Y. F. Lee, S. Punugupati, F. Wu, Z. Jin, J. Narayan and J. Schwartz, *Curr. Opin. Solid State Mater. Sci.*, 2014, **18**, 279–285.

49   V. Mourik, K. Zuo, S. M. Frolov, S. R. Plissard, E. P. A. M. Bakkers and L. P. Kouwenhoven, *Science*, 2012, **336**, 1003–1007.
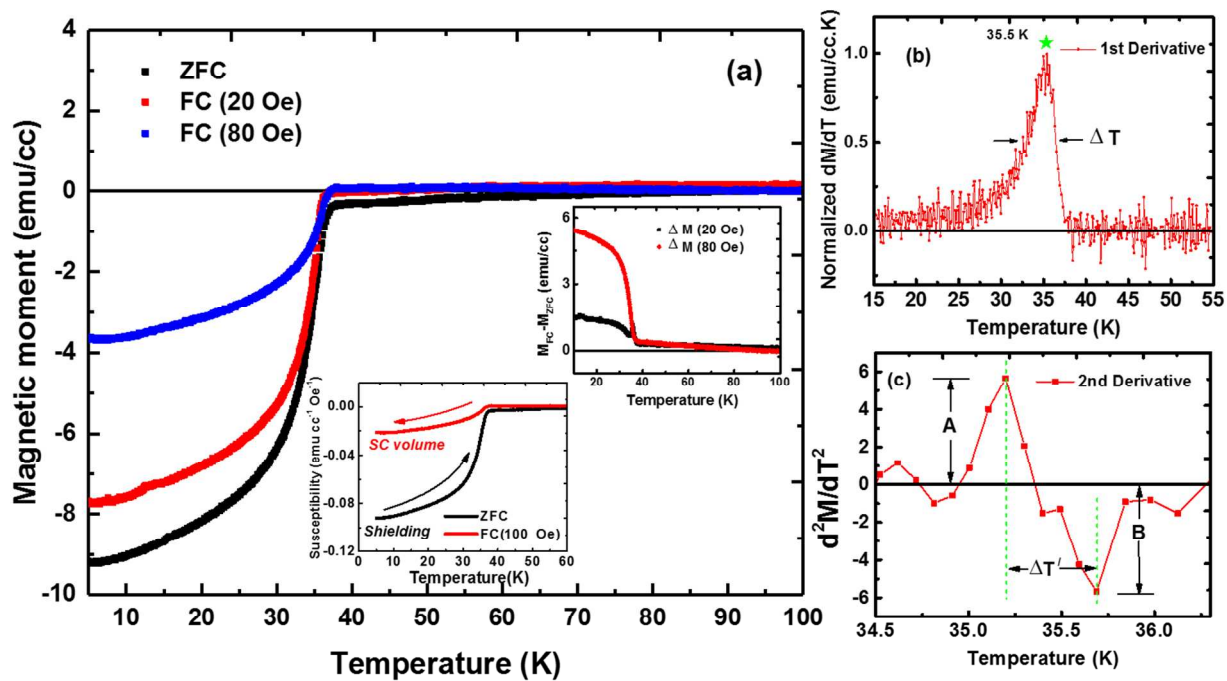
Figures:

Figure 1: (a) Magnetic moment *vs* temperature plots of B-doped Q-carbon at zero-field cooled (ZFC) and field cooled (FC) conditions; (b) The normalized first derivative of magnetic moment *vs* temperature showing T_c=35.5 K and Δ T=3 K; and (c) The second derivative of magnetic moment *vs* temperature. The insets in (a) show the temperature-dependent difference of FC and ZFC at 20 and 80 Oe and susceptibility *vs* temperature of B-doped Q-carbon.
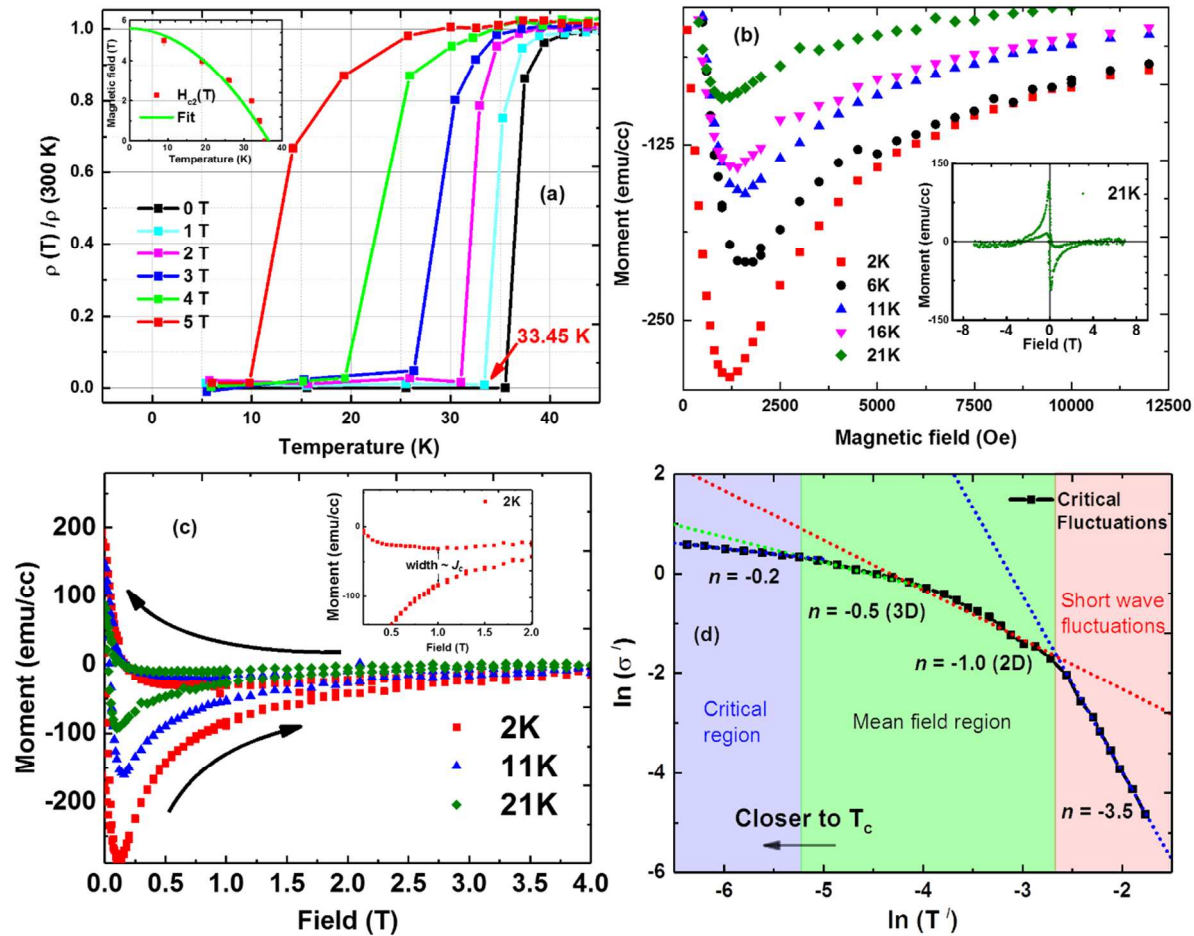
Figure 2: (a) Normalized resistivity *vs* temperature plots of B-doped Q-carbon at different applied fields (0, 1, 2, 3, 4 and 5 T); (b) Moment *vs* magnetic field plots at various temperatures (2, 6, 11, 16 and 21 K); (c) M *vs* H loops showing an irreversibility nature; and (d) Critical fluctuations in B-doped Q-carbon showing the crossover between 2D to 3D region. The insets in (a), (b), and (c) show variation of upper critical field with temperature, moment *vs* field at 21 K, and calculation of J_c, respectively.
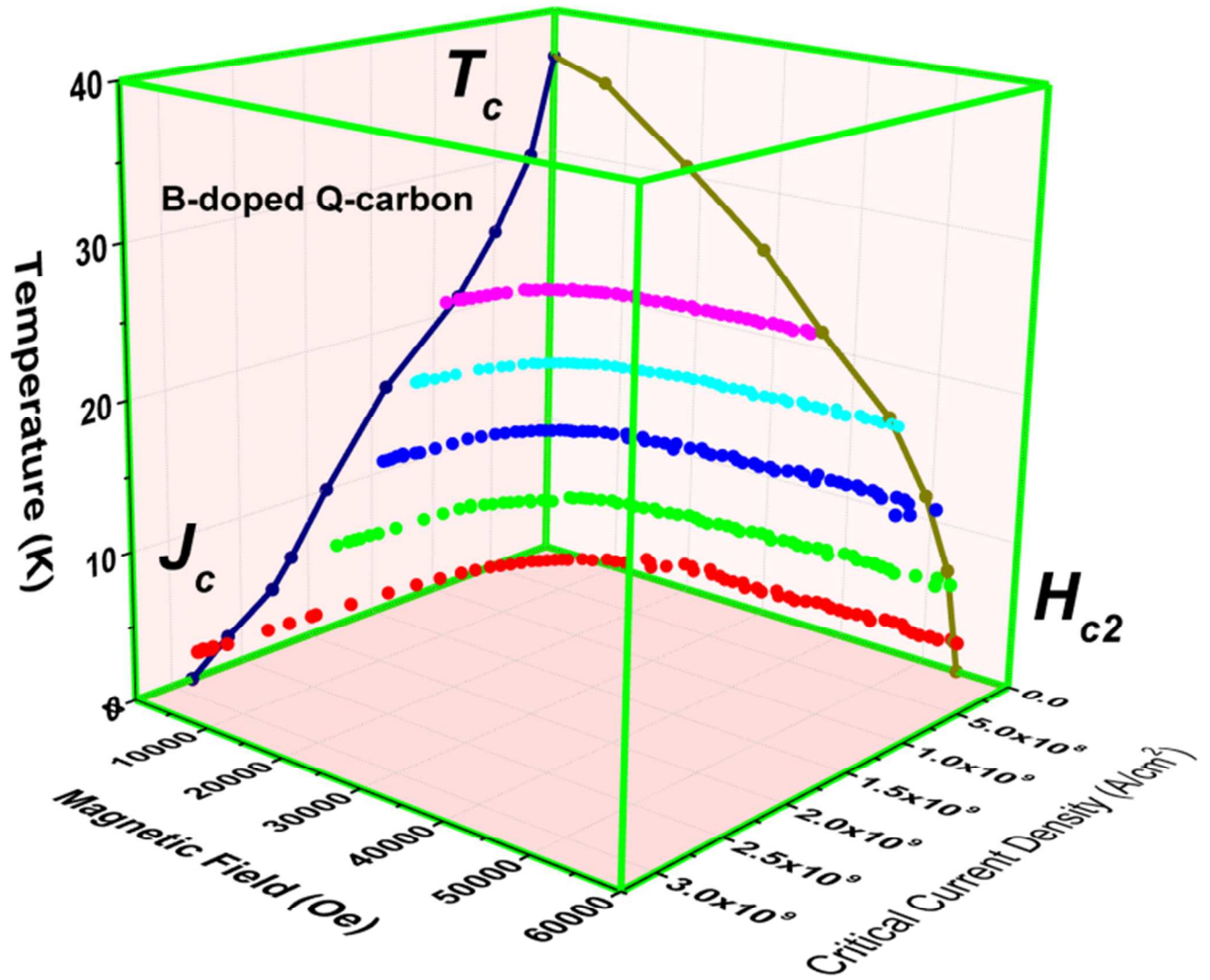
Figure 3: Superconducting region plot showing T_c, J_c and H_c in B-doped Q-carbon.
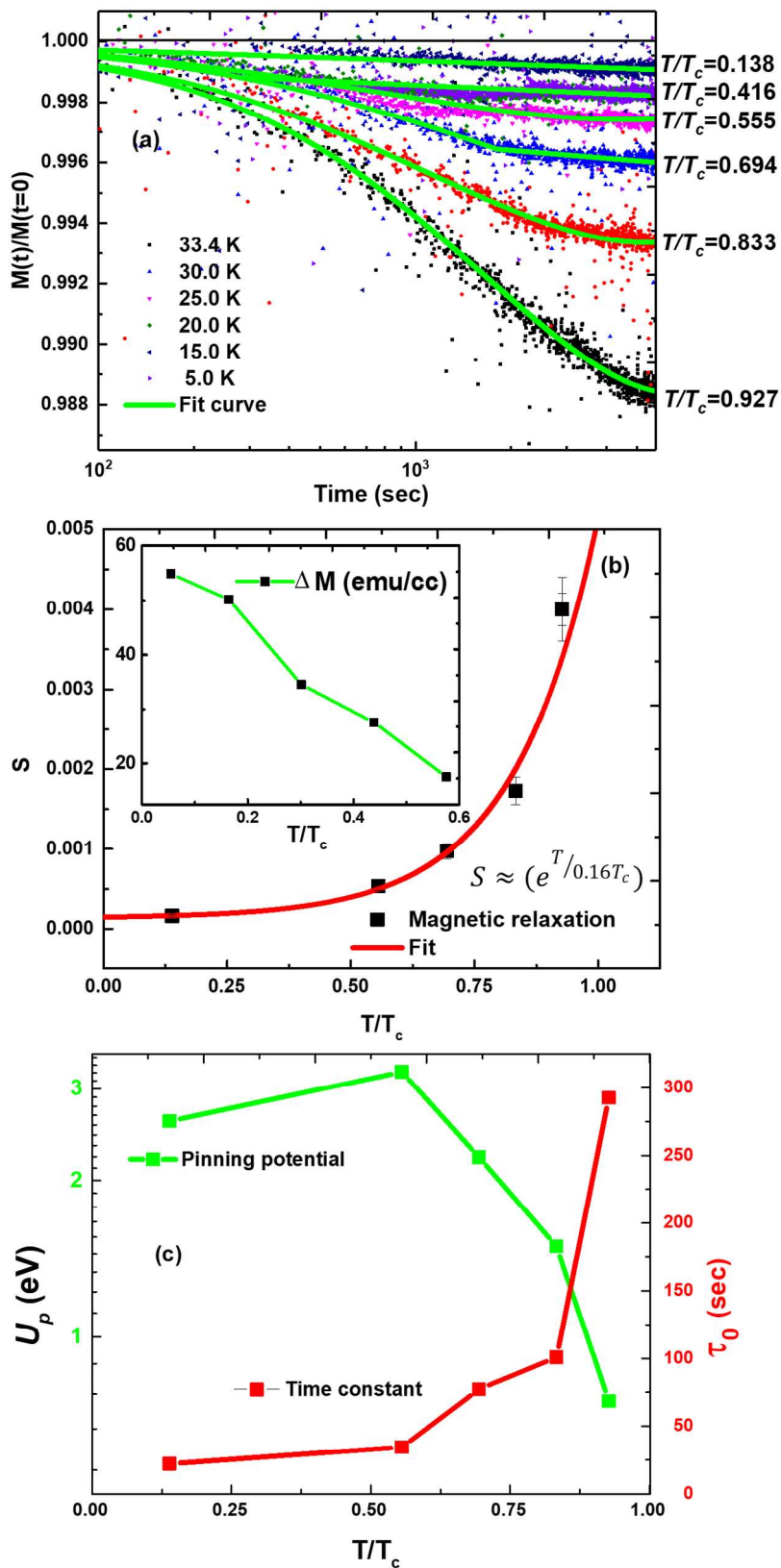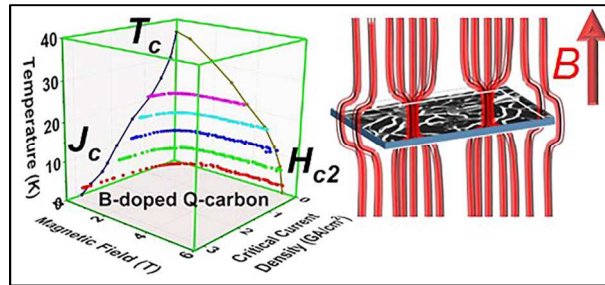
Figure 4: (a) Time-dependent magnetic moment at 1 T; (b) Magnetic relaxation *vs* T/T_c with the inset showing ΔM *vs* T/T_c ; and (c) Pinning potential and time constant *vs* T/T_c.

Three-dimensional critical fluctuations and Anderson-Kim logarithmic magnetic relaxations in B-doped Q-carbon high-temperature superconductor will lead to multifunctional high-speed electronic devices.